
Unveiling structure-property correlations in ferroelectric $\text{Hf}_{0.5}\text{Zr}_{0.5}\text{O}_2$ films using variational autoencoders

Kévin Alhada-Lahbabi¹ Brice Gautier¹ Damien Deleruyelle¹ Grégoire Magagnin¹

¹INSA Lyon, CNRS, Ecole Centrale de Lyon, Université Claude Bernard Lyon 1, CPE Lyon, INL, UMR5270, 69621 Villeurbanne, France.

Abstract

While $\text{Hf}_{0.5}\text{Zr}_{0.5}\text{O}_2$ (HZO) thin films hold significant promise for modern nanoelectronic devices, a comprehensive understanding of the interplay between their polycrystalline structure and electrical properties remains elusive. Here, we present a novel framework combining phase-field (PF) modeling with Variational Autoencoders (VAEs) to uncover structure-property correlations in polycrystalline HZO. Leveraging PF simulations, we constructed a high-fidelity dataset of P - V loops by systematically varying critical material parameters, including grain size, polar grain fraction, and crystalline orientation. The VAEs effectively encoded hysteresis loops into a low-dimensional latent space, capturing electrical properties while disentangling complex material parameters interdependencies. We further demonstrate a VAE-based inverse design approach to optimize P - V loop features, enabling the tailored design of device-specific key performance indicators (KPIs), including coercive field, remanent polarization, and loop area. The proposed approach offers a pathway to systematically explore and optimize the material design space for ferroelectric nanoelectronics.

1. Introduction

Ferroelectric materials have been foundational in information and communication technologies for decades, with the first commercial FeRAMs (Ferroelectric Random-Access Memories) emerging in the 1990s. These perovskite-based devices demonstrated low-voltage, energy-efficient switching, consuming only 1-10 fJ/bit—up to three orders of magnitude lower than other memory technologies.¹ However, their scalability has been limited to the 130 nm technology node, and their chemical incompatibility with CMOS technology hindered further advancements.² In contrast, fluorite-structured ferroelectrics, such as $\text{Hf}_{0.5}\text{Zr}_{0.5}\text{O}_2$ (HZO), have emerged as promising candidates for next-generation devices due to their compatibility with CMOS³ and their demonstrated ferroelectricity in ultra-thin films (below a thickness of 2 nm).⁴

Despite these advantages, HZO-based ferroelectric devices face critical challenges, including wake-up, fatigue, and imprint. Wake-up refers to the gradual improvement in polarization states during initial cycling, while fatigue describes the eventual degradation of these states, reducing the device's endurance and reliability.⁵ Imprint, characterized by the shift in polarization hysteresis loops due to charge trapping or internal electric fields, further exacerbates variability and impacts long-term stability. These phenomena are intricately linked to nanoscale structural features such as grain boundaries, phase heterogeneities, and local defects,

resulting in inconsistent performance across devices even under identical processing conditions.

To address these challenges, a multi-scale characterization framework is essential, bridging nanoscale material behavior with macroscopic device performance. Such an approach can correlate structural features like grain size, interfaces, and phase composition with device metrics such as endurance, retention, and coercive field. The complexity and non-linearity of these relationships pose significant challenges for conventional analytical methods. Recent advances in unsupervised machine learning, have demonstrated the potential to uncover latent physical mechanisms through variational autoencoders, offering transformative solutions for linking material behavior across scales.^{6,7}

VAEs are particularly well-suited for handling high-dimensional, multi-scale data. They compress complex datasets into a low-dimensional latent space, uncovering hidden patterns and key variables driving material behavior.^{8,9} This allows for the identification of critical correlations between nanoscale properties and macroscopic performance, such as the impact of grain size distribution on fatigue resistance or the role of phase heterogeneity in wake-up behavior. Furthermore, VAEs enable predictive modeling by exploring the latent space to identify optimal configurations for desired device properties,¹⁰ such as finding initial film parameters that maximize remnant polarization for increasing a device memory window and/or minimize the coercive

fields to reduce the device energy consumption.^{11,12}

The optimal film parameters for ferroelectric memory devices depend heavily on the specific device architecture and target application. For example, in Ferroelectric Field-Effect Transistors (FeFETs), minimizing leakage currents and optimizing the interface quality between the ferroelectric layer and the channel is critical for achieving high endurance and retention.¹³ Similarly, for neuromorphic applications, controlling the polarization dynamics to attain stable, multi-level resistance states is crucial for mimicking synaptic behavior.^{14,15} By leveraging the latent space of VAEs, it becomes possible to tailor film properties to meet the specific performance requirements of each device type, enabling more targeted and efficient material optimization.

High-throughput phase-field (PF) simulations have become fundamental for understanding ferroelectric materials, particularly $\text{Hf}_{0.5}\text{Zr}_{0.5}\text{O}_2$ (HZO)-based devices.^{16,17,18} Recent studies have modeled ferroelectric hysteresis in HZO^{19,20,21,22,23,24,25} and analyzed the effects of polycrystalline grain structures on electrical properties.^{26,27} Phase-field modeling has also been applied to investigate electric-field-induced phase transitions,²⁸ spacer layer impacts on domain dynamics,²⁹ and the role of oxygen vacancies in electrical behavior.^{30,31,32} PF modeling thus enables the generation of high-fidelity datasets capturing polarization evolution and field-induced dynamics in HZO thin films.

In this work, we first leverage PF modeling to simulate a wide range of material parameter distributions, such as variations in grain size, phase fraction, and defect distributions, to generate rich datasets for training the VAE. Next, we demonstrate how the VAE latent space disentangles the complex interplay of these material parameters and their impact on HZO’s electrical properties. Finally, we illustrate the inverse design of ferroelectric hysteresis properties using the VAE framework. This integration of PF simulation and VAE facilitates systematic exploration of the material design space, offering valuable guidance for experimental efforts to optimize functional properties.

2. Results

2.1. Material Parameter space

In this study, our primary objective is to investigate how the interaction between key material parameters governing polycrystalline structures influences the electrical properties of HZO, utilizing PF modeling and VAE. Specifically, we aim to explore the impact of four critical parameters that dictate the crystalline arrangement: the average grain size (D_G), the proportion of orthombic polar to monoclinic non-polar grains (ν_{ortho}), the preferential orientation of the crystallographic axis (μ_θ), and the dispersion of grain orientations relative to this axis (σ_θ).

In **Figure 1a**, three examples of $10\text{ nm} \times 128\text{ nm}$ 2D polycrystalline structures, generated via Voronoi tessellation, are presented, each corresponding to a distinct combination of material parameters $[D_G, \nu_{ortho}, \mu_\theta, \sigma_\theta]$. These structures exhibit various grain arrangements based on the average grain size D_G (here ranging from 10 nm to 20 nm), encompassing both equiaxed and columnar grains. The polarization vector field, initialized in a downward orientation, is represented by white arrows, illustrating the interplay between the fiber texture μ_θ and the grain orientation dispersion σ_θ , as well as their effect on the grain orientation distribution θ_G . Furthermore, non-polar grains are depicted in black, indicating a polarization fraction ranging from 100% to 60%. The corresponding ferroelectric hysteresis loops, obtained from PF simulations, are shown alongside, highlighting the influence of crystalline parameters on the electrical properties of HZO. Specifically, the coercive field E_c , remanent polarization P_r , loop area, and saturation polarization P_S exhibit significant variation with changes in the polycrystalline structure, revealing a complex relationship between the material parameters and the resulting P - V loops.

To elucidate the structure-property correlations in ferroelectric $\text{Hf}_{0.5}\text{Zr}_{0.5}\text{O}_2$, we employ a VAE, as illustrated in **Figure 1b**. A dataset of 10,000 PF P - V loops is generated by sampling various combinations of material parameters $[D_G, \nu_{ortho}, \mu_\theta, \sigma_\theta]$ (see Methods). The VAE takes the polarization points of the ferroelectric hysteresis loops as input \mathbf{x} , encodes them into a 2D latent space, and decodes them to reconstruct the original P - V loops. Subsequently, a predictive model, chosen here as Gaussian Processes (GPs), is trained in a supervised manner to infer the material parameters from the latent variables, thereby linking the latent space to the original material parameter space.

2.2. VAE Latent Space Analysis

After training is complete, the 10,000 P - V loops comprising the datasets are represented in the VAE latent space in **Figure 2**, based on the two latent variables Z_1, Z_2 . Here, the latent representation of the ferroelectric hysteresis is color-coded based on their grain orientation dispersion (σ_θ) (**Figure 2a**), preferential crystalline orientation (μ_θ) (**Figure 2b**), polar grain fraction (ν_{ortho}) (**Figure 2c**), and average grain size (D_G) (**Figure 2d**), allowing to elucidate the correlation between the material properties and VAE encoding. Additionally, the latent manifold resulting from the reconstruction of a continuous square of dimensions $[-2, 2] \times [-2, 2]$ in the latent space is shown in **Figure 2e** offering a continuous representation of the encoded hysteresis behaviors. This manifold highlights the VAE’s structured organization of the latent space, where P - V loops are predominantly arranged based on their remanent polarization, saturation polarization, coercive field, loop area, and shape

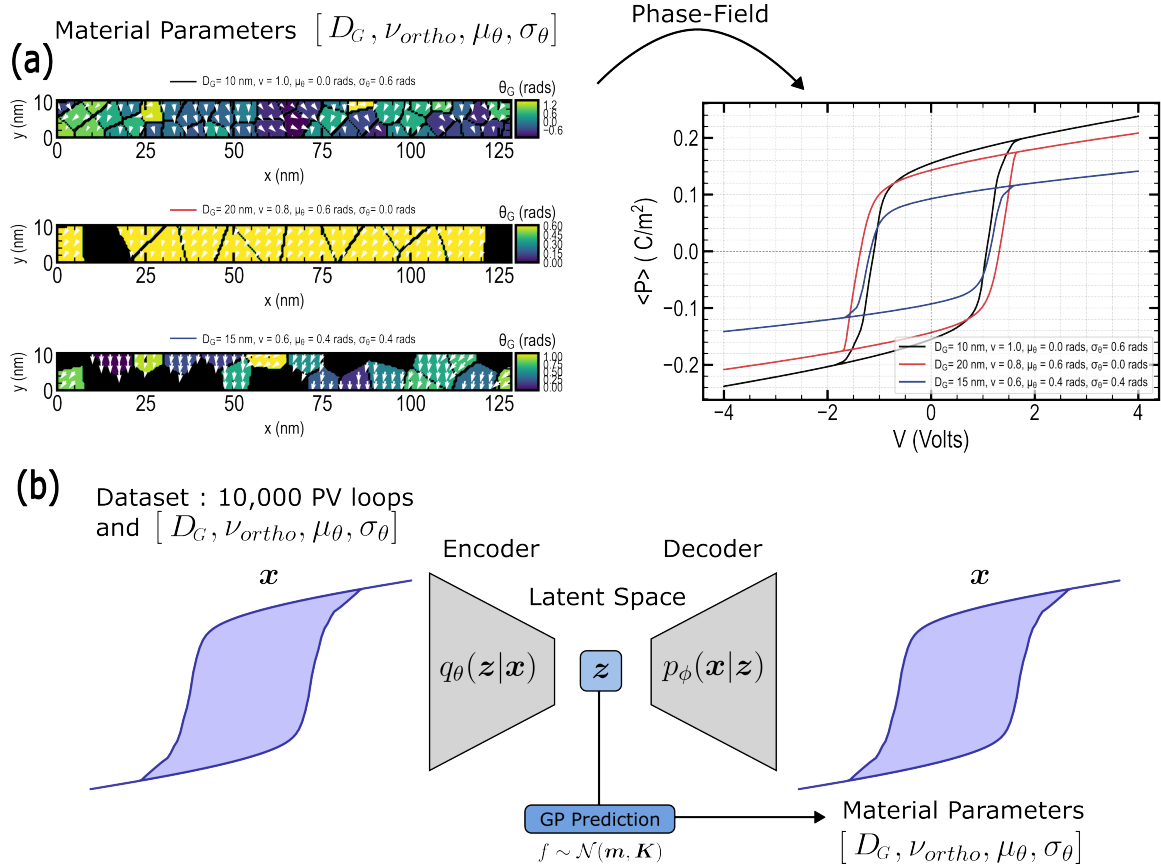


Figure 1. Schematic Workflow for Using VAE to Disentangle Material Parameters' Influence on HZO Ferroelectric Hysteresis. (a) Three polycrystalline structures, each with a unique set of material parameters—grain size (D_G), grain orientation dispersion (σ_θ), preferential crystalline orientation (μ_θ), and polar grain fraction (ν_{ortho})—and their corresponding P - V loops from PF modeling. Grain orientation is color-coded, with white arrows representing polarization direction, and black regions corresponding to non-polar grains and grain boundaries. (b) The VAE workflow, encoding P - V loops into a 2D latent space and decoding them. GPs predict the material parameters from the latent variables, connecting the latent space to the original material property space.

across the dataset.

The VAE representation effectively captures the relationship between material parameters and P - V loop features, as organized within the latent space. For instance, the grain orientation dispersion (σ_θ) shows minimal correlation with the latent variables, with no discernible clusters or organization in the latent space. This suggests a limited influence on the P - V loop characteristics compared to other material parameters, further supported by its relatively low Pearson correlation coefficients ($r_{Z_1} = -0.11$, $r_{Z_2} = 0.21$), as depicted in Figure 3 (see Methods). In contrast, the preferential crystallographic orientation (μ_θ) exhibits a stronger correlation, particularly with the Z_2 latent variable ($r_{Z_2} = 0.47$). This dependency is evident in the latent manifold, where μ_θ values near 0 (corresponding to a vertically aligned c-axis) are concentrated in the lower quadrant, resulting in more open P - V loops with higher coercive fields. This behavior arises from the enhanced coupling between polarization and

the vertical electric field when the c-axis aligns with the out-of-plane direction. The polar fraction (ν_{ortho}) demonstrates a strong correlation with Z_1 ($r_{Z_1} = 0.63$), as reflected in the latent manifold, where increases in ν_{ortho} correspond to higher remanent and saturation polarization along the Z_1 axis. Finally, the average grain size (D_G) shows significant correlation with both Z_1 and Z_2 ($r_{Z_1} = 0.59$ and $r_{Z_2} = 0.56$, respectively). Larger grain sizes in the latent space are associated with higher remanent and saturation polarization, as well as increased loop opening and coercive field values.

To further explore the VAE latent representation, the latent space is visualized in Figure 4, with color coding based on features extracted from the reconstructed P - V loops. Specifically, the coercive field (E_c) (Figure 4a), remanent polarization (P_r) (Figure 4b), hysteresis loop area (Figure 4c), and saturation polarization (P_s) (Figure 4d) were derived from the decoded latent points. Remarkably, these P - V features exhibit a smooth and continuous variation

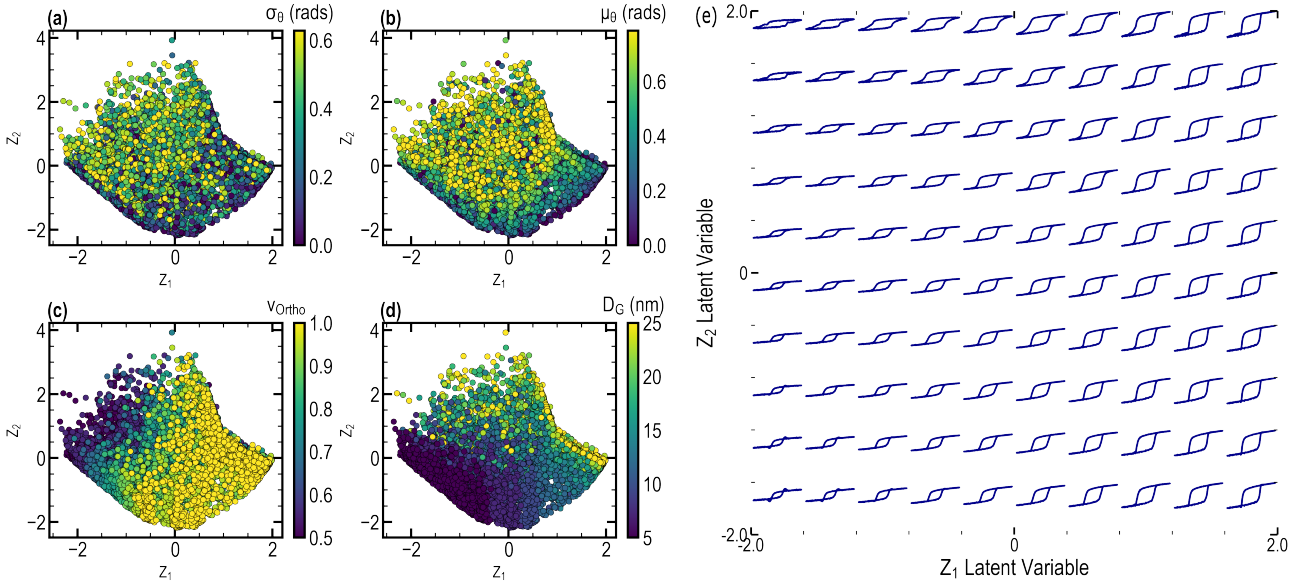


Figure 2. Representation of the Ferroelectric Hysteresis Dataset in the VAE Latent Space. The 2D latent space (Z_1, Z_2) of the VAE is used to represent the latent encoding of ferroelectric hysteresis data. Each point in the latent space corresponds to a hysteresis loop, with the points colored by the material properties used to generate the respective polarization-voltage (P - V) loops. The material properties include: (a) grain orientation dispersion (σ_θ), (b) preferential crystalline orientation (μ_θ), (c) polar grain fraction (ν_{ortho}), and (d) average grain size (D_G). Additionally, (e) the latent manifold is constructed by decoding points sampled uniformly within the $[-2, 2] \times [-2, 2]$ square in the latent space.

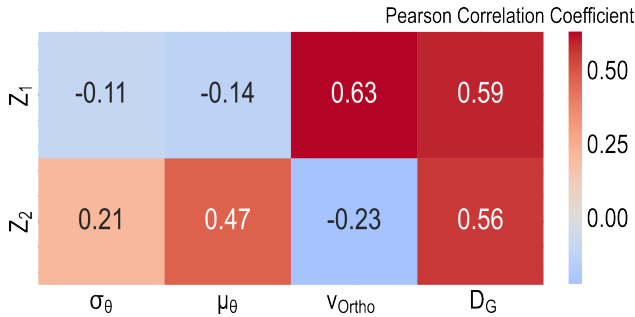


Figure 3. Pearson Correlation Coefficient Between Latent Variables and Material Properties. Pearson correlation coefficients between the 2D latent variables (Z_1, Z_2) derived from the VAE encoding and the material properties associated with the ferroelectric hysteresis loops: grain orientation dispersion (σ_θ), preferential crystalline orientation (μ_θ), polar grain fraction (ν_{ortho}), and average grain size (D_G).

across the latent space, highlighting the VAE’s ability to disentangle and organize key hysteresis properties effectively. This continuity not only underscores the model’s efficiency in representing P - V loop features but also opens avenues for generating and inversely designing P - V loops with specified properties, leveraging the latent space’s struc-

tured representation.

2.3. VAE for the Inverse Design of Ferroelectric Hysteresis

Using the proposed VAE-based approach, the inverse design of ferroelectric hysteresis with targeted properties becomes possible through the generation of realistic P - V loops from the learned latent space. Specifically, P - V loops with a specified range for the coercive field, remanent polarization, saturation polarization, and loop area, can be obtained, fulfilling the requirement specific to different applications.

To demonstrate the potential of the inverse design approach, we seek to identify a ferroelectric hysteresis loop in the latent space with specific feature characteristics. The desired properties are arbitrarily chosen as follows: a coercive field (E_c) between 1.4 and 1.6 MV/cm, remanent polarization (P_r) between 0.15 and 0.25 C/m², saturation polarization (P_s) between 0.20 and 0.26 C/m², and a hysteresis loop area ranging from 1 to 1.5 a.u.

To locate a region in the VAE latent space that meets these criteria, we continuously decode the $[-2, 2] \times [-2, 2]$ square region and extract the corresponding P - V loop characteristics. This results in a continuous mapping from the latent space to the P - V properties, as illustrated in **Figure 5**. By

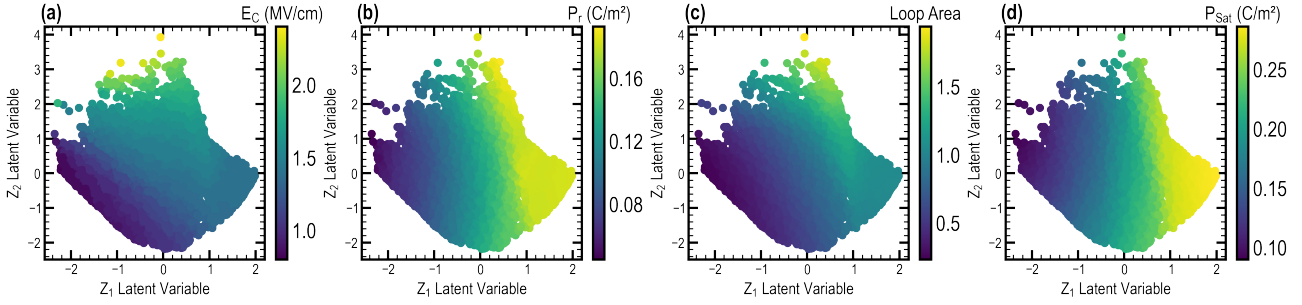


Figure 4. Representation of the evolution Ferroelectric Hysteresis Properties within the VAE Latent. The 2D latent space (Z_1, Z_2) derived from the VAE encoding is visualized with color-coded subplots corresponding to key ferroelectric hysteresis loop properties: (a) coercive field (E_c), (b) remanent polarization (P_r), (c) hysteresis loop area, and (d) saturation polarization (P_s).

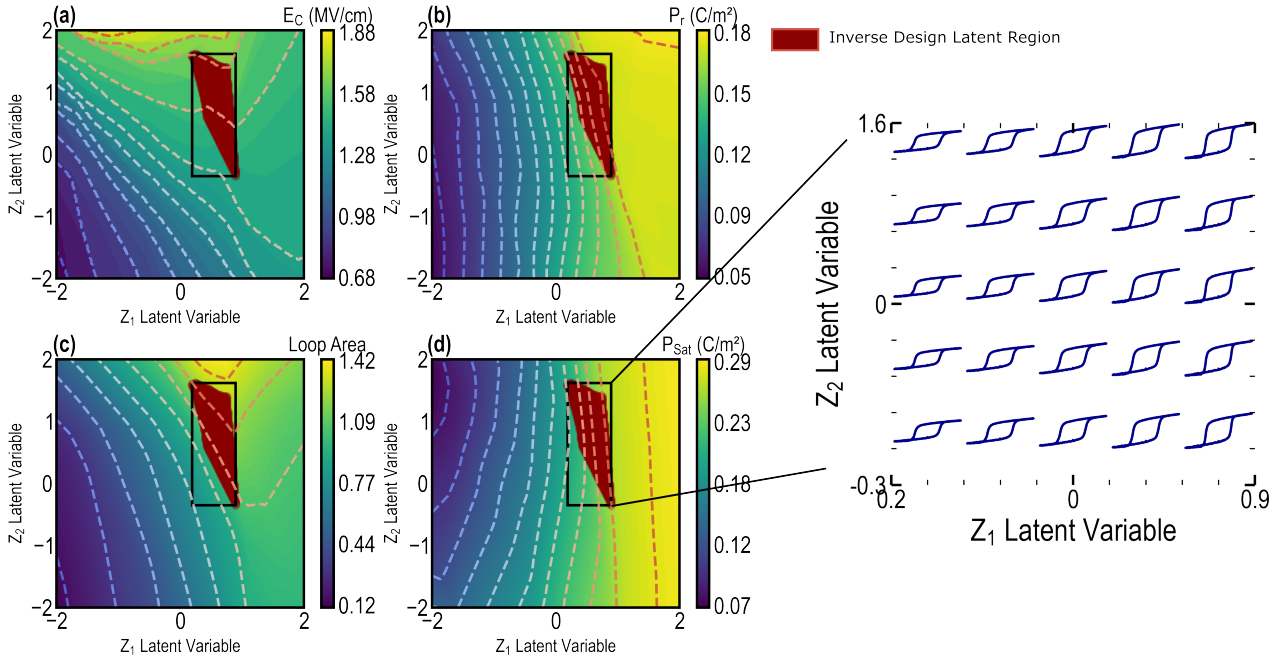


Figure 5. Inverse Design of P - V Features from VAE Latent Space Decoding. Ferroelectric hysteresis properties, including (a) coercive field (E_c), (b) remanent polarization (P_r), (c) loop area, and (d) saturation polarization (P_s), obtained by decoding the $[-2, 2] \times [-2, 2]$ latent space. The red region highlights latent points whose decoded P - V loops satisfy the inverse design criteria for E_c , loop area, P_r , and P_s . The manifold representation within the $[0.2, 0.9] \times [-0.3, 1.6]$ black rectangle illustrates ferroelectric hysteresis loops that meet the specified design requirements.

analyzing this mapping, we can identify the latent region that satisfies the specified requirements. In this case, the region of interest is highlighted in red on the 2D latent space. Furthermore, a representation of the generated P - V loop manifold in the vicinity of this region, within the latent coordinates $[0.2, 0.9] \times [-0.3, 1.6]$, is shown in Figure 5e, where the recovered ferroelectric hysteresis loops fulfill the design specifications.

Finally, the material parameters corresponding to the fer-

roelectric hysteresis generated from the VAE latent space must be recovered to complete the inverse design process. While the VAE can effectively generate samples from latent regions different from the training points to a certain extent, reconstructing the material parameters requires the mapping of the latent space to the material parameters $[D_G, \nu_{ortho}, \mu_\theta, \sigma_\theta]$. This step may be challenging, especially if the material parameter do not exhibit a significant correlation with the latent variables.

Here, we employ GPs to map the latent variables Z_1, Z_2 to the material parameters $[D_G, \nu_{\text{ortho}}, \mu_{\theta}, \sigma_{\theta}]$ (see Methods):

$$f_{\text{GP}}([Z_1, Z_2]) = [D_G, \nu_{\text{ortho}}, \mu_{\theta}, \sigma_{\theta}]$$

where f_{GP} represents the GP model that predicts the material parameters from the latent variables. Notably, a separate GP model was trained for each material parameter. The GP prediction of the material parameters over the $[-2, 2] \times [-2, 2]$ latent space is depicted in **Figure 6**.

The GPs can be further utilized to predict the material parameters corresponding to the latent region that satisfies the design requirements. For instance, by inputting the latent point $Z = (0.8, 0.5)$ which is present in this inverse design region, the GP model predicts the following material parameters: average grain size $D_G = 16.2$ nm, polar fraction $\nu_{\text{ortho}} = 0.87$, preferential crystalline orientation $\mu_{\theta} = 0.54$ rads, and grain orientation dispersion $\sigma_{\theta} = 0.38$ rads. It is important to note that the predictions made by the GPs are inherently associated with uncertainty, allowing for the determination of confidence intervals for the predicted material parameters. These intervals provide bounds on the reliability of the predictions. The standard deviations associated with the predictions are as follows: $\sigma_{D_G} = 3.4$ nm, $\sigma_{\nu_{\text{ortho}}} = 0.09$, $\sigma_{\mu_{\theta}} = 0.15$ rads, and $\sigma_{\sigma_{\theta}} = 0.15$ rads.

Finally, the recovered material parameters are utilized to generate the polycrystalline structure and the corresponding phase-field P - V loop, as presented in **Figure 7**. The simulated P - V loop demonstrates the following characteristics: coercive field $E_c = 1.44$ MV/cm, loop area of 1.2 a.u., remanent polarization $P_r = 0.18$ C/m², and saturation polarization $P_s = 0.26$ C/m², all of which align with the specified design criteria. These outcomes underscore the successful implementation of the inverse design methodology in achieving the targeted P - V loop properties.

3. Discussion

In this study, we introduced an approach based on VAEs and PF modeling of polycrystalline $\text{Hf}_{0.5}\text{Zr}_{0.5}\text{O}_2$ to elucidate the interplay between the polycrystalline structure and the electrical properties of the material.

The usefulness of the proposed VAE-based inverse design approach lies in its ability to identify key material parameters that directly influence the performance of ferroelectric devices. By mapping the latent space to specific features of the P - V loop, such as coercive field, remnant polarization, and loop area, the framework enables the optimization of these properties to meet specific device requirements. For example, in FeFETs, minimizing the coercive field and maximizing remnant polarization is critical to reducing energy consumption and increasing memory window.¹³ This inverse design framework allows for targeted exploration

of the polycrystalline HZO parameter space, optimizing variables such as grain size, polar grain fraction, and crystallographic orientation to achieve desired electrical properties. The ability to recover and predict material parameters from the latent space provides a systematic pathway to tailor the polycrystalline structure for device-specific KPIs. For instance, reducing imprint voltage or mitigating fatigue effects can be targeted by precisely adjusting the grain size distribution or polar fraction in the functional film.

VAEs are a powerful tool for disentangling the complex relationships between material parameters in the PF modeling of polycrystalline HZO. This method provides valuable insights into the interdependencies of these parameters. Furthermore, we introduced an inverse design framework that leverages the continuous generative capabilities of the VAE, combined with GPs, to design ferroelectric hysteresis loops with specific properties and recover the corresponding material parameters governing the polycrystalline structure.

The Landau coefficients were arbitrarily chosen for this study and remain constant across the dataset. It is crucial to note that the KPIs, such as remanent and saturation polarization magnitudes, are significantly influenced by the Landau coefficients. While this study primarily focuses on the impact of the polycrystalline structure, it is also possible to investigate the interplay between the polycrystalline structure and the Landau coefficients with the VAE approach. Additionally, the inverse design approach could be extended to calibrate these Landau coefficients, which remains an actual challenge for polycrystalline HZO ferroelectrics.

However, the computational demands of generating large PF simulation datasets for VAE training remain a challenge. Although, integrating ML surrogates, such as graph neural networks or transfer learning models, can significantly accelerate data generation.^{33,34,35,36} These ML surrogates could be incorporated into the VAE framework to efficiently generate a more diverse and comprehensive dataset, potentially extending to 3D PF simulations and enabling the inclusion of additional parameters, such as film thickness, or dielectric layer properties, further enhancing the design space and predictive power of the framework.

Moreover, the flexibility of this framework extends beyond hysteresis loop properties. It can be adapted to optimize other material response characteristics, such as butterfly loop behavior, fatigue resistance, or frequency-dependent switching dynamics. This broad applicability makes the approach highly valuable for advancing ferroelectric devices across diverse applications, from memory and logic to energy storage and neuromorphic computing.

In conclusion, we introduced an ML framework combining VAEs and phase-field modeling to provide a robust and versatile tool for elucidating structure-property relationships

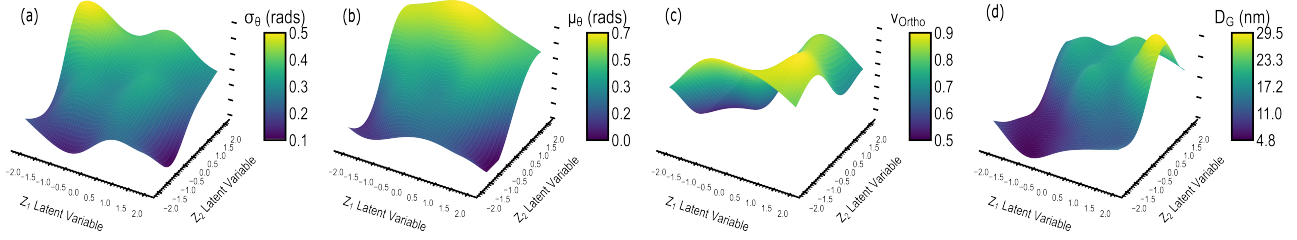


Figure 6. GP Predictions of Material Properties in the VAE Latent Space. GP regression of material properties from the 2D latent space (Z_1, Z_2) derived from the VAE. Predictions were made across a $[-2, 2] \times [-2, 2]$ square in the latent space for the (a) grain orientation dispersion (σ_θ), (b) preferential crystalline orientation (μ_θ), (c) polar grain fraction (ν_{ortho}), and (d) average grain size (D_G).

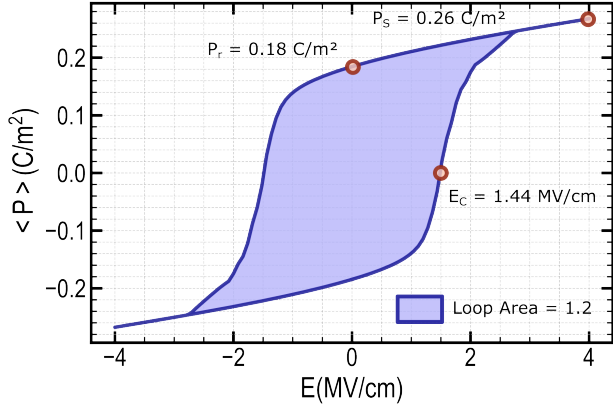


Figure 7. P - V Loop Modeled from Voronoi Structure Based on Material Parameters from VAE Inverse Design. The ferroelectric hysteresis P - V loop is simulated using a PF model, with material parameters derived from the VAE inverse design process. The generated loop meets the predefined design requirements, reflecting the influence of the material parameters on the P - V characteristics.

in ferroelectric HZO thin films. By enabling the inverse design of material parameters tailored to device-specific KPIs, this approach paves the way for systematic and efficient optimization of next-generation ferroelectric devices.

4. Methods

4.1. Phase-Field Modeling

In this study, we utilized PF simulations to explore how material parameters of polycrystalline $\text{Hf}_{0.5}\text{Zr}_{0.5}\text{O}_2$ influence its electrical properties, building on the framework presented in recent research efforts.^{33,37} Key factors analyzed were the average grain diameter (D_G), the fraction of polar orthorhombic grains (ν_{ortho}), the preferential crystalline axis orientation (μ_θ), and the dispersion of grain orientations (σ_θ).

Simulations were conducted on a 2D grid ($10 \text{ nm} \times 128 \text{ nm}$) with a uniform spacing of $\Delta x = \Delta y = 0.5 \text{ nm}$. Polycrystalline structures were generated via Voronoi tessellation based on specified average grain diameters D_G . Grain boundaries, sampled uniformly between 1 nm and 2 nm, align with values commonly reported in the literature.^{38,39,40}

Ferroelectric grain orientations were modified by assigning a random angle θ_G to each grain, which defines the orientation of its polarization axis relative to the vertical direction. The corresponding rotation matrix \hat{R} was used to compute the free energy in the local crystalline coordinate system. This matrix transforms a global vector $\mathbf{r} = (x, y)$ into its local representation $\mathbf{r}^L = (x^L, y^L)$ as $\mathbf{r}^L = \hat{R}\mathbf{r}$:

$$\hat{R} = \begin{bmatrix} \cos(\theta_G(\mathbf{r})) & -\sin(\theta_G(\mathbf{r})) \\ \sin(\theta_G(\mathbf{r})) & \cos(\theta_G(\mathbf{r})) \end{bmatrix}.$$

To analyze the interplay between general crystalline texturing μ_θ (e.g., preferential orientations such as [001] or [111]) and the dispersion of grain orientations σ_θ , grain angles were sampled from a Gaussian distribution with a mean orientation μ_θ and standard deviation σ_θ ($\theta_G(\mathbf{r}) \sim \mathcal{N}(\mu_\theta, \sigma_\theta)$).

Additionally, the influence of the distribution of polar and non-polar grains within the crystalline structure was considered by varying the ratio of orthorhombic ferroelectric grains ν_{ortho} . For each polycrystalline structure, a fraction of $1 - \nu_{ortho}$ grains was randomly selected to be non-polar, representing the non-ferroelectric proportion of the polycrystalline system.

The evolution of the spontaneous polarization $P_i(\mathbf{r}, t)$ is given by the time-dependent Landau Ginzburg (TDGL) equation¹⁷:

$$\frac{\partial P_i(\mathbf{r}, t)}{\partial t} = -L_0 \frac{\delta F}{\delta P_i(\mathbf{r}, t)}, \quad (i = 1, 2) \quad (1)$$

where L_0 is a kinetic coefficient and F is the total free

energy, which includes the different energetic contributions,

$$F = \int_V (f_{\text{Landau}} + f_{\text{grad}} + f_{\text{electric}} + f_{\text{elastic}}) dV \quad (2)$$

where f_{Landau} , f_{grad} , f_{electric} , and f_{elastic} are the bulk, gradient, electric, and elastic free energy density, respectively.

In the polar $\text{Hf}_{0.5}\text{Zr}_{0.5}\text{O}_2$ grains, the polarization was assumed to be directed along the c-axis of the crystal, as commonly considered in HZO PF literature,^{26,41} with each grain's orientation θ_G taken into account. In this configuration, the bulk free energy is described by the Landau expansion:

$$f_{\text{Landau}} = \alpha_1 P_1^2 + \alpha_{11} P_1^4 + \alpha_{111} P_1^6$$

where P_1 represents the out-of-plane polarization aligned with the grain c-axis, and α_1 , α_{11} , and α_{111} are the Landau coefficients.

The energy contribution from domain walls is described by the gradient energy, assumed to be isotropic. It can be expressed as:

$$f_{\text{grad}} = G_{11} (P_{1,1}^2 + P_{2,2}^2) + G_{12} (P_{1,1}P_{2,2}) + \frac{1}{2} G_{44} [(P_{1,2} + P_{2,1})^2] + \frac{1}{2} G'_{44} [(P_{1,2} - P_{2,1})^2]. \quad (3)$$

where G_{ijkl} are the gradient energy coefficients, and $P_{i,j}$ denotes the partial derivative $\frac{\partial P_i}{\partial x_j}$.

The electrostatic energy is given by:

$$f_{\text{electric}} = -P_i E_i - \frac{1}{2} \epsilon_0 \epsilon_r E_i E_j$$

where E_i is the electric field, ϵ_0 is the vacuum permittivity, and ϵ_r is the relative dielectric permittivity. The electric field $E_i(\mathbf{r}) = -\frac{\partial V(\mathbf{r})}{\partial x_i}$ is derived from the electrostatic potential V , which satisfies the electrostatic equilibrium equation:

$$\frac{\partial}{\partial x_i} \left[\epsilon_0 \epsilon_r(\mathbf{r}) \frac{\partial V(\mathbf{r})}{\partial x_j} \right] = \frac{\partial P_i(\mathbf{r})}{\partial x_i} - \rho(\mathbf{r})$$

Here, ρ is the charge density, and $\frac{\partial P_i}{\partial x_i}$ is the polarization charge density. The electrostatic equilibrium is solved using the fast Fourier transform iterative spectral method with periodic boundary conditions in the in-plane directions and Dirichlet boundary conditions in the out-of-plane direction.⁴²

The elastic energy density is given by:

$$f_{\text{elastic}} = \frac{1}{2} C_{ijkl} (\epsilon_{ij}(\mathbf{r}) - \epsilon_{ij}^0(\mathbf{r})) (\epsilon_{kl}(\mathbf{r}) - \epsilon_{kl}^0(\mathbf{r}))$$

where C_{ijkl} is the elastic stiffness tensor, $\epsilon_{ij}(\mathbf{r})$ is the total strain, and $\epsilon_{ij}^0(\mathbf{r}) = Q_{ijkl} P_k(\mathbf{r}) P_l(\mathbf{r})$ is the electrostrictive

strain induced by the polarization, with Q_{ijkl} being the electrostrictive tensor.

The mechanical equilibrium equation is:

$$C_{ijkl} \frac{\partial^2 u_k(\mathbf{r})}{\partial x_j \partial x_l} = C_{ijkl} \frac{\partial \epsilon_{kl}^0(\mathbf{r})}{\partial x_j}$$

where u_k represents the mechanical displacements, determined using thin-film mechanical boundary conditions,^{16,29} with substrate and air layer thicknesses of $12\Delta x$ and $2\Delta x$, respectively.

To model the behavior of non-ferroelectric regions, such as non-polar grains and grain boundaries, the polarization was not governed by the TDGL equation. Instead, it was assumed to evolve as:

$$P_i(\mathbf{r}, t) = \epsilon_0(\epsilon_r - 1) E_i(\mathbf{r}, t), \quad (i = 1, 2)$$

consistently with previous studies on polycrystalline ferroelectric PF models.⁴³

Ferroelectric hysteresis was obtained using a uniformly discretized voltage ramp with 400 steps, ranging from -4 to 4 volts. At each step, a constant voltage was applied for $50\Delta t$. The electrostatic potential u_T at the top electrode was adjusted such that $V(x_{\text{top}}, y, z) = u_T$, while the bottom electrode was grounded with $V(0, y, z) = 0$ V. The average polarization $\langle P(V) \rangle$ was recorded at each step, resulting in 400 data points per P-V loop.

The Landau coefficients were selected as $\alpha_1 = -7.79 \times 10^8 \text{ C}^{-2} \text{ m}^2 \text{ N}$, $\alpha_{11} = 1.15 \times 10^{10} \text{ C}^{-4} \text{ m}^6 \text{ N}$, and $\alpha_{111} = -2.51 \times 10^{10} \text{ C}^{-6} \text{ m}^{10} \text{ N}$. The dielectric permittivity for HZO was set as $\epsilon_r^G = 30$ in the grains,⁴⁴ and an arbitrary lower value of $\epsilon_r^{GB} = 12$ was chosen for the grain boundaries. The remaining coefficients for the PF simulation were taken from Ref.²⁹ The time step was set as $\Delta t = 0.06t_0$, where $t_0 = 1/(\alpha_0 L_0)$.

To investigate the interplay between the material parameters governing the polycrystalline structure, the average grain diameter D_G , the polar orthorhombic fraction ν_{ortho} , crystalline fiber texture μ_θ , and crystalline orientation deviation σ_θ were varied in the simulations, as outlined in **Table 1**. Each parameter was discretized into 10 steps, resulting in a total of 10,000 PF simulations of ferroelectric hysteresis.

Parameters	D_G [nm]	ν_{ortho} [a.u.]	μ_θ [rads]	σ_θ [rads]
	$5 \sim 25$	$0.5 \sim 1$	$0 \sim \frac{\pi}{4}$	$0 \sim \frac{\pi}{5}$

Table 1. Range of material parameters related to the polycrystalline structure used in the PF simulations, including average grain diameter D_G , polar orthorhombic fraction ν_{ortho} , crystalline fiber texture μ_θ , and crystalline orientation deviation σ_θ .

4.2. Variational Autoencoder

In this work, we employed a VAE to learn a compact, low-dimensional representation of ferroelectric hysteresis generated by PF simulations. A VAE is a generative model consisting of an encoder $q_\theta(\mathbf{z}|\mathbf{x})$, which encodes the input sample \mathbf{x} into a latent representation \mathbf{z} , and a decoder $p_\phi(\mathbf{x}|\mathbf{z})$, which reconstructs the input from the latent space. Here, θ and ϕ are the parameters of the encoder and decoder, respectively. We specifically use a β -VAE,⁴⁵ where the evidence lower bound (ELBO) is maximized during training:

$$\mathcal{L}_{\theta,\phi}(\beta, \mathbf{x}, \mathbf{z}) = \mathbb{E}_{q_\phi(\mathbf{z}|\mathbf{x})}[\log p_\theta(\mathbf{x}|\mathbf{z})] - \beta D_{\text{KL}}(q_\phi(\mathbf{z}|\mathbf{x})||p(\mathbf{z}))$$

The first term represents the reconstruction loss, computed using binary cross-entropy, while the second term is the Kullback-Leibler (KL) divergence between the approximate posterior $q(\mathbf{z}|\mathbf{x})$ and the prior $p(\mathbf{z})$, assumed to be a standard normal distribution $\mathcal{N}(0, 1)$. The hyperparameter β controls the trade-off between reconstruction quality and latent space regularization.

Both the encoder and decoder were implemented as multi-layer perceptrons (MLPs) with one hidden layer consisting of 256 units, and the latent dimension was set to 2. The β coefficient was set to 0.1, and the model was trained for 200 epochs with a batch size of 128 and a learning rate of 10^{-3} using the Adam optimizer.

4.3. Pearson Correlation Coefficient

The Pearson correlation coefficient (r) is a statistical measure used to quantify the linear relationship between two variables. In this study, r is employed to evaluate the correlation between the VAE latent variables (Z_1, Z_2) and the material parameters or P - V loop characteristics. The Pearson correlation coefficient ranges from -1 to 1 , with values closer to -1 or 1 indicating a stronger negative or positive linear relationship, respectively, and values near 0 suggesting no linear correlation. The coefficient r is calculated using the formula:

$$r = \frac{\text{Cov}(x, y)}{\sigma_x \sigma_y}$$

where $\text{Cov}(x, y)$ represents the covariance between the variables x and y , and σ_x and σ_y denote the standard deviations of x and y , respectively.

4.4. Gaussian Processes

GPs are a nonparametric supervised learning method widely utilized for regression tasks. Here, the objective is to learn the function f that maps inputs $\mathbf{x} = [Z_1, Z_2]$ (2D latent coordinates) to outputs $\mathbf{y} = [D_G, \nu_{\text{ortho}}, \mu_\theta, \sigma_\theta]$ (material parameters), given a set of observations $\mathbf{Y} = \{y_1, y_2, \dots, y_n\}$ at corresponding input points $\mathbf{X} = \{\mathbf{x}_1, \mathbf{x}_2, \dots, \mathbf{x}_n\}$.

The GP prior over the latent function values $f = \{f(\mathbf{x}_1), f(\mathbf{x}_2), \dots, f(\mathbf{x}_n)\}$ is formally expressed as:

$$f \sim \mathcal{N}(m(\mathbf{X}), K(\mathbf{X}, \mathbf{X}))$$

where \mathcal{N} denotes a multivariate normal distribution, $m(\mathbf{X})$ is the mean vector, and $K(\mathbf{X}, \mathbf{X})$ is the covariance matrix with entries $k(\mathbf{x}_i, \mathbf{x}_j)$ defined by a kernel function. The radial basis function (RBF) kernel is chosen here, given by:

$$k_{\text{RBF}}(\mathbf{x}_i, \mathbf{x}_j) = \sigma^2 \exp\left(-\frac{|\mathbf{x}_i - \mathbf{x}_j|^2}{2l^2}\right)$$

where σ^2 is the variance, and l is the length scale of the kernel. In addition to the RBF kernel, we used a White kernel, defined as:

$$k_W(\mathbf{x}_i, \mathbf{x}_j) = \sigma_n^2 \delta_{ij}$$

where σ_n^2 represents the noise variance, which is set to 0.005, and δ_{ij} is the Kronecker delta function. The kernel parameters were optimized during training using 1,000 randomly selected training points, comprising 2D latent encodings $\mathbf{X} = [Z_1, Z_2]$ and their corresponding labels $\mathbf{Y} = [D_G, \nu_{\text{ortho}}, \mu_\theta, \sigma_\theta]$. Notably, an independent GP was trained for the prediction of each label.

Data availability

The data that support the findings of this study are available from the corresponding authors upon reasonable request.

Acknowledgements

This work has received the financial support of IPCEI France 2030 Programs POI and eFerroNVM together with ANR-23-CE24-0015-01 ECHOES project.

Author Contributions

Kévin Alhada-Lahbabi: Conceptualization (equal); Data curation (equal); Formal analysis (equal); Investigation (equal); Methodology (equal); Writing – review & editing (equal).

Brice Gautier: Conceptualization (equal); Funding acquisition (equal); Resources (equal); Supervision (equal); Validation (equal); Writing – review & editing (equal).

Damien Deleruyelle: Conceptualization (equal); Funding acquisition (equal); Resources (equal); Supervision (equal); Validation (equal); Writing – review & editing (equal).

Grégoire Magagnin: Conceptualization (equal); Supervision (equal); Validation (equal); Data curation (equal); For-

mal analysis (equal); Investigation (equal); Methodology (equal); Project administration (equal); Writing – review & editing (equal)

Competing Interests

The authors declare no competing interests.

References

- ¹ Asif Islam Khan, Ali Keshavarzi, and Suman Datta. The future of ferroelectric field-effect transistor technology. *Nature Electronics*, 3:588–597, 10 2020.
- ² Daisaburo Takashima. Overview of ferams: Trends and perspectives. In *2011 11th Annual Non-Volatile Memory Technology Symposium Proceeding*, pages 1–6, 2011.
- ³ Halid Mulaosmanovic, Evelyn T Breyer, Stefan Dünkler, Sven Beyer, Thomas Mikolajick, and Stefan Slesazek. Ferroelectric field-effect transistors based on HfO₂: a review. *Nanotechnology*, 32:502002, 12 2021.
- ⁴ Suraj S. Cheema, Daewoong Kwon, Nirmaan Shanker, Roberto dos Reis, Shang-Lin Hsu, Jun Xiao, Haigang Zhang, Ryan Wagner, Adhiraj Datar, Margaret R. McCarter, Claudy R. Serrao, Ajay K. Yadav, Golnaz Karbasian, Cheng-Hsiang Hsu, Ava J. Tan, Li-Chen Wang, Vishal Thakare, Xiang Zhang, Apurva Mehta, Evguenia Karapetrova, Rajesh V Chopdekar, Padraic Shafer, Elke Arenholz, Chenming Hu, Roger Proksch, Ramamoorthy Ramesh, Jim Ciston, and Sayeef Salahuddin. Enhanced ferroelectricity in ultrathin films grown directly on silicon. *Nature*, 581:E5–E5, 5 2020.
- ⁵ Franz Fegler, Min Hyuk Park, Tony Schenk, Milan Pešić, and Uwe Schroeder. Field Cycling Behavior of Ferroelectric HfO₂-Based Capacitors. pages 381–398. Elsevier, 2019.
- ⁶ Sergei V. Kalinin, Rama Vasudevan, Yongtao Liu, Ayana Ghosh, Kevin Roccapiore, and Maxim Ziatdinov. Probe microscopy is all you need, 6 2023.
- ⁷ Yongtao Liu, Bryan D Huey, Maxim A Ziatdinov, and Sergei V Kalinin. Physical discovery in representation learning via conditioning on prior knowledge: applications for ferroelectric domain dynamics, 2024.
- ⁸ Sergei V. Kalinin, James J. Steffes, Yongtao Liu, Bryan D. Huey, and Maxim Ziatdinov. Disentangling ferroelectric domain wall geometries and pathways in dynamic piezoresponse force microscopy via unsupervised machine learning. *Nanotechnology*, 33, 1 2022.
- ⁹ Yongtao Liu, Maxim Ziatdinov, and Sergei V. Kalinin. Exploring causal physical mechanisms via non-gaussian linear models and deep kernel learning: Applications for ferroelectric domain structures. *ACS Nano*, 16:1250–1259, 1 2022.
- ¹⁰ Carl Doersch. Tutorial on variational autoencoders. 6 2016.
- ¹¹ Yongtao Liu, Roger Proksch, Chun Yin Wong, Maxim Ziatdinov, and Sergei V. Kalinin. Disentangling ferroelectric wall dynamics and identification of pinning mechanisms via deep learning. *Advanced Materials*, 33, 10 2021.
- ¹² Aditya Raghavan, Rohit Pant, Ichiro Takeuchi, Eugene A. Eliseev, Marti Checa, Anna N. Morozovska, Maxim Ziatdinov, Sergei V. Kalinin, and Yongtao Liu. Evolution of ferroelectric properties in smxbl-xfeo₃ via automated piezoresponse force microscopy across combinatorial spread libraries. *ACS Nano*, 9 2024.
- ¹³ Hanxue Jiao, Xudong Wang, Shuaiqin Wu, Yan Chen, Junhao Chu, and Jianlu Wang. Ferroelectric field effect transistors for electronics and optoelectronics. *Applied Physics Reviews*, 10(1), 2023.
- ¹⁴ Min-Kyu Kim, Youngjun Park, Ik-Jyae Kim, and Jang-Sik Lee. Emerging materials for neuromorphic devices and systems. *Iscience*, 23(12), 2020.
- ¹⁵ Ik-Jyae Kim and Jang-Sik Lee. Ferroelectric transistors for memory and neuromorphic device applications. *Advanced Materials*, 35(22):2206864, 2023.
- ¹⁶ Y. L. Li, S. Y. Hu, Z. K. Liu, and L. Q. Chen. Effect of substrate constraint on the stability and evolution of ferroelectric domain structures in thin films. *Acta Mater.*, 50(2):395–411, 2002.
- ¹⁷ Long-Qing Chen. Phase-field models for microstructure evolution. *Annual Review of Materials Research*, 32(1):113–140, 2002.
- ¹⁸ Yuhong Zhao. Understanding and design of metallic alloys guided by phase-field simulations. *npj Computational Materials*, 9:94, 2023.
- ¹⁹ Prabhat Kumar, Andrew Nonaka, Revathi Jambunathan, Girish Pahwa, Sayeef Salahuddin, and Zhi Yao. FerroX: A GPU-accelerated, 3D phase-field simulation framework for modeling ferroelectric devices. *Computer Physics Communications*, 290:108757, 2023.
- ²⁰ Atanu K. Saha, Kai Ni, Sourav Dutta, Suman Datta, and Sumeet Gupta. Phase field modeling of domain dynamics and polarization accumulation in ferroelectric HZO. *Applied Physics Letters*, 114(20):202903, 2019.
- ²¹ A. K. Saha, M. Si, K. Ni, S. Datta, P. D. Ye, and S. K. Gupta. Ferroelectric Thickness Dependent Domain Interactions in FEFETs for Memory and Logic: A Phase-field

-
- Model based Analysis. In *2020 IEEE International Electron Devices Meeting (IEDM)*, pages 4.3.1–4.3.4, 2020.
- ²² Pingan Zhou, Binjian Zeng, Wanzhen Yang, Jiajia Liao, Fanqi Meng, Qinghua Zhang, Lin Gu, Shuaizhi Zheng, Min Liao, and Yichun Zhou. Intrinsic 90° charged domain wall and its effects on ferroelectric properties. *Acta Materialia*, 232:117920, 2022.
- ²³ Michael Hoffmann, Mengcheng Gui, Stefan Slesazek, Riccardo Fontanini, Mattia Segatto, David Esseni, and Thomas Mikolajick. Intrinsic Nature of Negative Capacitance in Multidomain $Hf_{0.5}Zr_{0.5}O_2$ -Based Ferroelectric/Dielectric Heterostructures. *Advanced Functional Materials*, 32(2):2108494, 2022.
- ²⁴ Xin Wen, Mattia Halter, Laura Bégon-Lours, and Mathieu Luisier. Physical modeling of HZO-based ferroelectric field-effect transistors with a WO_x channel. *Frontiers in Nanotechnology*, 4:900592, 2022.
- ²⁵ Alhada-Lahbabi Kévin, Deleruyelle Damien, and Gautier Brice. Ultrafast and accurate prediction of polycrystalline hafnium oxide phase-field ferroelectric hysteresis using graph neural networks. *Nanoscale Adv.*, 6:2350–2362, 2024.
- ²⁶ Sandeep Sugathan, Krishnamohan Thekkepat, Soumya Bandyopadhyay, Jiyoung Kim, and Pil Ryung Cha. A phase field model combined with a genetic algorithm for polycrystalline hafnium zirconium oxide ferroelectrics. *Nanoscale*, 14(40):14997–15009, 2022.
- ²⁷ R. Koduru, A. K. Saha, M. Si, X. Lyu, P. D. Ye, and S. K. Gupta. Variation and Stochasticity in Polycrystalline HZO based MFIM: Grain-Growth Coupled 3D Phase Field Model based Analysis. In *2021 IEEE International Electron Devices Meeting (IEDM)*, pages 15.2.1–15.2.4, 2021.
- ²⁸ Zhaobo Liu, Xiaoming Shi, Jing Wang, and Houbing Huang. Electric-field-induced crystallization of $Hf_{0.5}Zr_{0.5}O_2$ thin film based on phase-field modeling. *npj Quantum Materials*, 9(1):44, 2024.
- ²⁹ Ren-Ci Peng, Shubin Wen, Xiaoxing Cheng, Long-Qing Chen, Min Liao, and Yichun Zhou. Revealing the Role of Spacer Layer in Domain Dynamics of $Hf_{0.5}Zr_{0.5}O_2$ Thin Films for Ferroelectrics. *Advanced Functional Materials*, 34(40):2403864, 2024.
- ³⁰ Synergistic effect of strain and oxygen vacancy on the ferroelectric properties of hafnium oxide-based ferroelectric films. *Computational Materials Science*, 221:112036, 2023.
- ³¹ Jiajia Chen, Jiacheng Xu, Zhi Gong, Jiani Gu, Xiao Yu, Chengji Jin, Yue Peng, Yan Liu, Bing Chen, Ran Cheng, and Genquan Han. Controlling the Ferroelectricity of Doped- HfO_2 via Reversible Migration of Oxygen Vacancy. *IEEE Transactions on Electron Devices*, 70(4):1789–1794, 2023.
- ³² Shucheng Zhang, Yu Li, Yingfen Wei, Yize Sun, Xu-meng Zhang, Hao Jiang, and Qi Liu. A general physics model of oxygen vacancy dynamics for ferroelectricity enhancement and degradation in hafnia-based thin films. *IEEE Transactions on Electron Devices*, 71(11):6706–6712, 2024.
- ³³ Kévin Alhada-Lahbabi, Damien Deleruyelle, and brice Gautier. Ultrafast and accurate prediction of polycrystalline hafnium oxide phase-field ferroelectric hysteresis using graph neural networks. *Nanoscale Adv.*, pages –, 2024.
- ³⁴ Kévin Alhada-Lahbabi, Damien Deleruyelle, and Brice Gautier. Machine learning surrogate for 3d phase-field modeling of ferroelectric tip-induced electrical switching. *npj Computational Materials*, 10(1):197, 2024.
- ³⁵ David Montes de Oca Zapiain, James A. Stewart, and Rémi Dingreville. Accelerating phase-field-based microstructure evolution predictions via surrogate models trained by machine learning methods. *npj Comput. Mater.*, 7(1):1–11, 2021.
- ³⁶ Kévin Alhada-Lahbabi, Damien Deleruyelle, and Brice Gautier. Transfer learning for accelerating phase-field modeling of ferroelectric domain formation in large-scale 3d systems. *Computer Methods in Applied Mechanics and Engineering*, 429:117167, 2024.
- ³⁷ Kévin Alhada-Lahbabi, Damien Deleruyelle, and Brice Gautier. Phase-Field Study of Nanocavity-Assisted Mechanical Switching in $PbTiO_3$ Thin Films. *Advanced Electronic Materials*, page 2300744, 2024.
- ³⁸ M. Lederer, T. Kämpfe, R. Olivo, D. Lehninger, C. Mart, S. Kirbach, T. Ali, P. Polakowski, L. Roy, and K. Seidel. Local crystallographic phase detection and texture mapping in ferroelectric Zr doped HfO_2 films by transmission-EBSD. *Applied Physics Letters*, 115(22):22, 2019.
- ³⁹ Maxim G. Kozodaev, Anna G. Chernikova, Evgeny V. Korostylev, Min Hyuk Park, Roman R. Khakimov, Cheol S. Hwang, and Andrey M. Markeev. Mitigating wakeup effect and improving endurance of ferroelectric $HfO_2 - ZrO_2$ thin films by careful La-doping. *Journal of Applied Physics*, 125(3):034101, 01 2019.
- ⁴⁰ Takashi Onaya, Toshihide Nabatame, Mari Inoue, Yong Chan Jung, Heber Hernandez-Arriaga, Jaidah Mohan, Harrison Sejoon Kim, Naomi Sawamoto, Takahiro

-
- Nagata, Jiyoung Kim, and Atsushi Ogura. Improvement in ferroelectricity and breakdown voltage of over 20 nm thick $Hf_xZr_{1-x}O_2/ZrO_2$ bilayer by atomic layer deposition. *Applied Physics Letters*, 117(23):232902, 12 2020.
- ⁴¹ Hyeon Woo Park, Jangho Roh, Yong Bin Lee, and Cheol Seong Hwang. Modeling of negative capacitance in ferroelectric thin films. *Advanced Materials*, 31(32):1805266, 2019.
- ⁴² J. J. Wang, X. Q. Ma, Q. Li, J. Britson, and Long Qing Chen. Phase transitions and domain structures of ferroelectric nanoparticles: Phase field model incorporating strong elastic and dielectric inhomogeneity. *Acta Mater.*, 61(20):7591–7603, 2013.
- ⁴³ Patrick Fedeli, Federico Cuneo, Luca Magagnin, Luca Nobili, Marc Kamlah, and Attilio Frangi. On the simulation of the hysteresis loop of polycrystalline pzt thin films. *Smart Materials and Structures*, 29(9):095007, jul 2020.
- ⁴⁴ Min Hyuk Park, Han Joon Kim, Yu Jin Kim, Woongkyu Lee, Taehwan Moon, and Cheol Seong Hwang. Evolution of phases and ferroelectric properties of thin $Hf_{0.5}Zr_{0.5}O_2$ films according to the thickness and annealing temperature. *Applied Physics Letters*, 102(24):24, 2013.
- ⁴⁵ Christopher P Burgess, Irina Higgins, Arka Pal, Loic Matthey, Nick Watters, Guillaume Desjardins, and Alexander Lerchner. Understanding disentangling in β -vae. *arXiv preprint arXiv:1804.03599*, 2018.